3-D magnetotelluric inversion and model validation with gravity data for the investigation of flood basalts and associated volcanic rifted margins

Sophie Hautot, R.T. Single, J. Watson, N. Harrop, D.A. Jerram, Pascal Tarits, K. Whaler, G. Dawes

Geophys. J. Int. (2007) **170,** 1418–1430 doi: 10.1111/j.1365-246X.2007.03453.x

3-D magnetotelluric inversion and model validation with gravity data for the investigation of flood basalts and associated volcanic rifted margins

S. Hautot,[1,*] R. T. Single,[2,4] J. Watson,[3] N. Harrop,[3] D. A. Jerram,[4] P. Tarits,[1] K. Whaler[5] and G. Dawes[5]

[1] *IUEM-UBO, UMR CNRS 6538 'Domaines Océaniques', Place Nicolas Copernic,* 29280 *Plouzané, France*
[2] *Statoil A.S.A., Heidrun Petek,* PO Box 273, N-7501 *Stjørdal, Norway*
[3] *ARK Geophysics, Featherstone Road, Wolverton Mill, Milton Keynes* MK12 5EU, *UK*
[4] *University of Durham, Department of Earth Sciences, Science Laboratories, South Road, Durham* DH1 3LE, *UK*
[5] *School of GeoSciences, Grant Institute, The University of Edinburgh, West Mains Road, Edinburgh* EH9 3JW, *UK*

Accepted 2007 March 27. Received 2007 March 25; in original form 2005 May 25

SUMMARY

20 magnetotelluric (MT) soundings were collected on the Isle of Skye, Scotland to provide a high-resolution three-dimensional (3-D) electrical resistivity model of a volcanic province within the framework of a project jointly interpreting gravity, seismic, geological and MT data. The full 3-D inversion of the MT data jointly interpreted with gravity data reveals upper crustal structure. The main features of the model are interpreted in conjunction with previous geological mapping and borehole data. Our model extends to 13 km depth, several kilometres below the top of the Lewisian basement. The top of the Lewisian basement is at approximately 7–8 km depth and the topography of its surface was controlled by Precambrian rifting, during which a 4.5 km thick sequence of Torridonian sediments was deposited. The Mesozoic sediments above, which can reach up to 2.2 km thick, have small-scale depocentres and are covered by up to 600 m of Tertiary lava flows. The interpretation of the resistivity model shows that 3-D MT inversion is an appropriate tool to image sedimentary structures beneath extrusive basalt units, where conventional seismic reflection methods may fail.

Key words: 3-D inversion, gravity, magnetotellurics, rifted margin.

1 INTRODUCTION

Volcanic rifted margins represent up to 90 per cent of existing continental margins (Menzies *et al.* 2002). In many cases such margins are also intimately associated with flood basalts generating large volumes of volcanic cover over sediment and basement structures that developed prior to these eruptions. This volcanic cover and associated intrusions makes it very difficult to investigate the subsurface in such regions, often referred to as the 'subbasalt imaging problem' (e.g. Fliedner & White 2001; Jerram 2002; Single & Jerram 2004; Kumar *et al.* 2004; Martini *et al.* 2005). A better understanding of the subbasalt architecture is important because the pre-existing lithospheric structures in such regions are thought to play an important role in the location and intensity of magmatism in the volcanic rifted margins and flood basalt provinces (Ziegler & Cloetingh 2004). Also, such structures will define the location of sedimentary basins beneath the basalts which may have potential hydrocarbon reserves. Additionally, the intrusion of igneous material, and through flux of magma, potentially play a role in the thermal evolution of the sedimentary basin (Hinz *et al.* 1993), and can control the maturation of the sediments with implications for their resource potential (England *et al.* 1993). Given the importance of a better understanding of the subbasalt architecture and continued interest in exploration in offshore volcanic rifted margins, new approaches must be taken to probe the subvolcanic structure. One possible method of investigating the subsurface is by using magnetotellurics (MT). Full three-dimensional (3-D) inversion of MT data, although not commonly applied, has shown great potential for the characterisation of complex geological structures at different scales (Hautot *et al.* 1999, 2000). In this contribution, we consider the use of MT in the investigation of flood basalts, subbasalt basins and associated volcanic rifted margins. We have collected new MT data from the Isle of Skye, in the Sea of the Hebrides Basin, NW Scotland, which is an onshore example of flood basalt cover over sedimentary and basement structures. We show that 3-D MT inversion can provide a geological image of these complex structures hidden by thick basaltic cover. Additionally, the MT data also provide information about structures and features within the basalts. Small-scale features

*Previously at University of Edinburgh, UK.

in the resistivity model are interpreted by combining the MT results with gravity data, and it is shown that the combination of MT and gravity data is an important tool in subbasalt imaging.

2 GEOLOGICAL SETTING

The Isle of Skye, NW Scotland, is part of the British Palaeogene Igneous Province associated with the opening of the North Atlantic and the development of the much larger North Atlantic Igneous Province (NAIP). Onset of the NAIP around 62–61 Ma (Pearson *et al.* 1996; Hamilton *et al.* 1998) was widespread across Western Greenland, Eastern Greenland, and the British Tertiary and erupted over a number of sedimentary basins and basement settings (Jerram & Widdowson 2005). The Isle of Skye is situated in one such basin, the Sea of the Hebrides Basin (Fig. 1), and contains extensive exposures of flood volcanics overlying sediments and basement with good access, making it ideal for an MT study (Figs 1 and 2). Additionally, the area has been well documented in terms of its structure (e.g. Stein & Blundell 1990; Durham 2003), burial and uplift history (e.g. England *et al.* 1993), and its volcanic history and architecture (e.g. Williamson & Bell 1994; Single & Jerram 2004). The geological context of the Isle of Skye is complex. The continental crust underwent several lithospheric extension episodes before the Late Cretaceous rifting opening of the NW Atlantic, including in the pre-Cambrian (Torridonian) and lower Palaeozoic, and there were episodes of Triassic rifting, Jurassic subsidence and Late Cretaceous uplift (Stein & Blundell 1990; England *et al.* 1993).

The Sea of Hebrides basin was controlled by NNE–SSW faults and it was suggested that these faults are reactivated Precambrian structures (Stein & Blundell 1990) (Fig. 1a). The oldest formation is the Lewisian gneiss complex over which a thick sequence of Precambrian sediments was deposited in large fault-bounded basins (Torridonian). Successive sedimentary sequences in the Palaoezoic and Mesozoic were deposited in response to extension and reactivation of the major faults, resulting in a number of subbasins around the Inner and Outer Hebrides, with sediments of varying thicknesses, up to 3 s Two Way Traveltime (equivalent to ≈9 km thick, Blundell, private communication, 2007) thickening towards the down-thrown side of the basin bounding faults (Stein & Blundell 1990). In the study area, the northwestern Isle of Skye, thick basaltic lava flows of Tertiary age cover Mesozoic sedimentary basins (Fig. 2). The sedimentary basins developed during rifting episodes and were subsequently deformed tectonically and intruded by sills close to the contact between basalts and the sediments (England *et al.* 1993; Williamson & Bell 1994). The sediments are only observed at outcrops at a few locations along the coast; otherwise, they are entirely covered by basalt. They were deposited successively in fluvial (Trias), marine (Bajocian) and lagoonal (Bathonian) environments (Harris 1992).

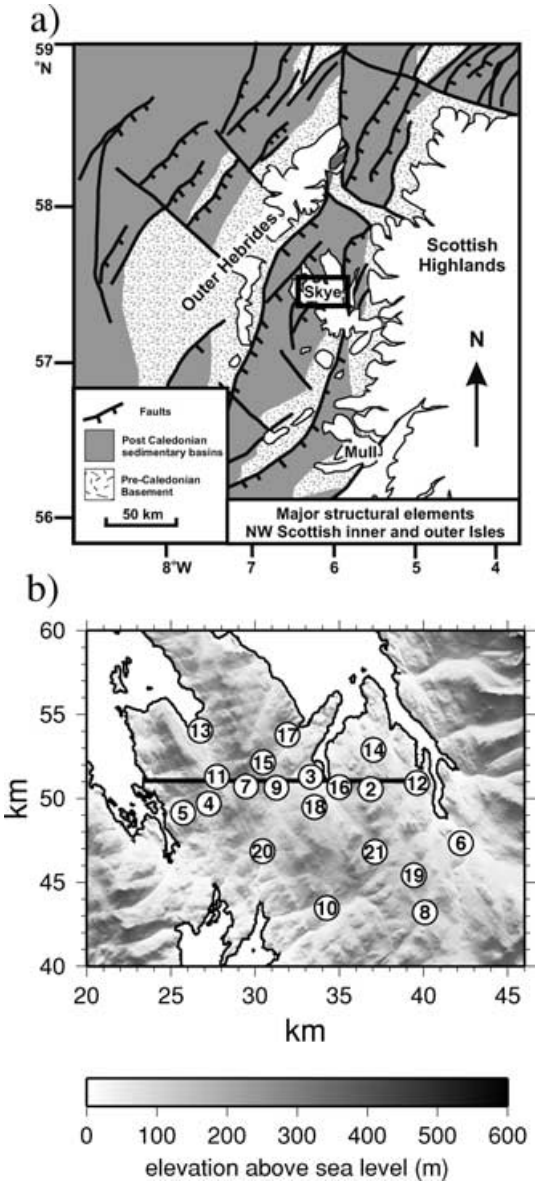

Figure 1. (a) Major structural elements around the Sea of Hebrides, NW Scotland, highlighting major rifted fault structures (reactivated from existing basement structure) and location of sedimentary basins (adapted from Stein & Blundell 1990). The box outlines the study area. (b) Shaded topographic relief map of northern Skye with location of the MT sites (numbered dots) and the gravity profile (black line).

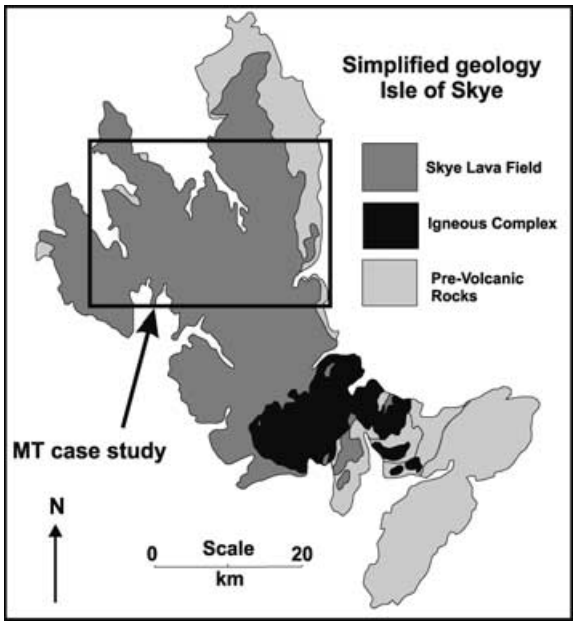

Figure 2. Simplified geological map of the Isle of Skye outlining the distribution of the main geological units.

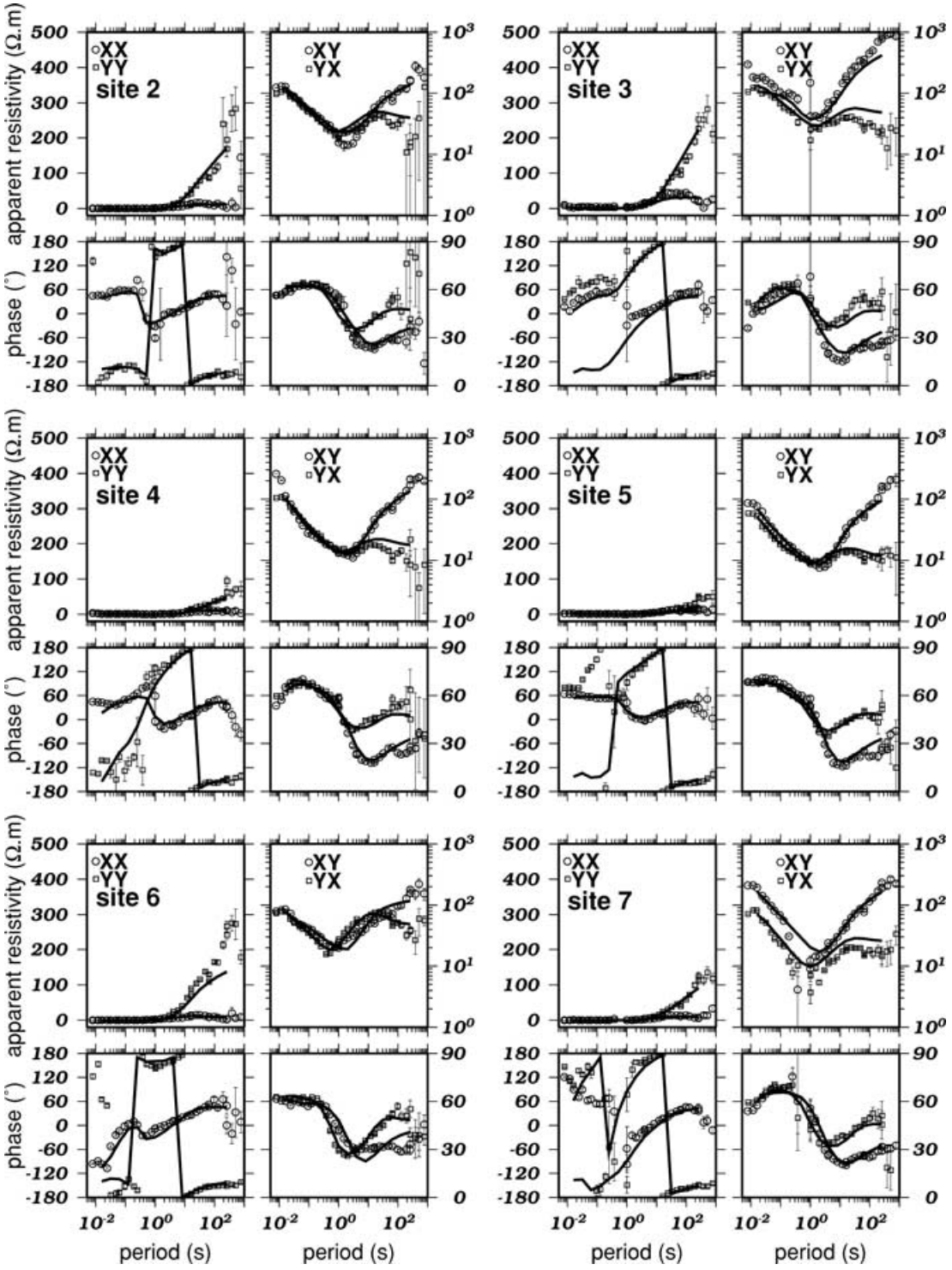

Figure 3. The MT impedance tensor at sites 2–7. Both the amplitude and phase of the diagonal (left, circles: xx; squares: yy) and off-diagonal (right, circles: xy; squares: yx) terms are shown. Amplitudes are expressed in apparent resistivity units (ohm m), and the error bars are one standard deviation. Note the change in vertical scale between the diagonal (linear) and off-diagonal (logarithmic) apparent resistivity terms, since the amplitudes of Z_{xx} and Z_{yy} are close to 0 at many sites and periods. The solid line is the impedance predicted by the best-fitting 3-D model. See Fig. 1(b) for the site locations.

3 MAGNETOTELLURIC SOUNDINGS

3.1 Survey and data processing

We carried out 20 MT soundings (Fig. 1) with the Short Period Automatic Magnetotelluric (SPAM) Mark III data acquisition system (Ritter *et al.* 1998) with Metronix broadband coils. The horizontal electric and magnetic field time-series were recorded in two frequency modes: the high frequency bands (2048-8 Hz) and the longer period bands (128-2048 s). The electric potentials were measured between two non-polarizable $Cl_2 - PbCl_2$ electrodes with a typical separation of 50 m. Electric and magnetic fields were recorded

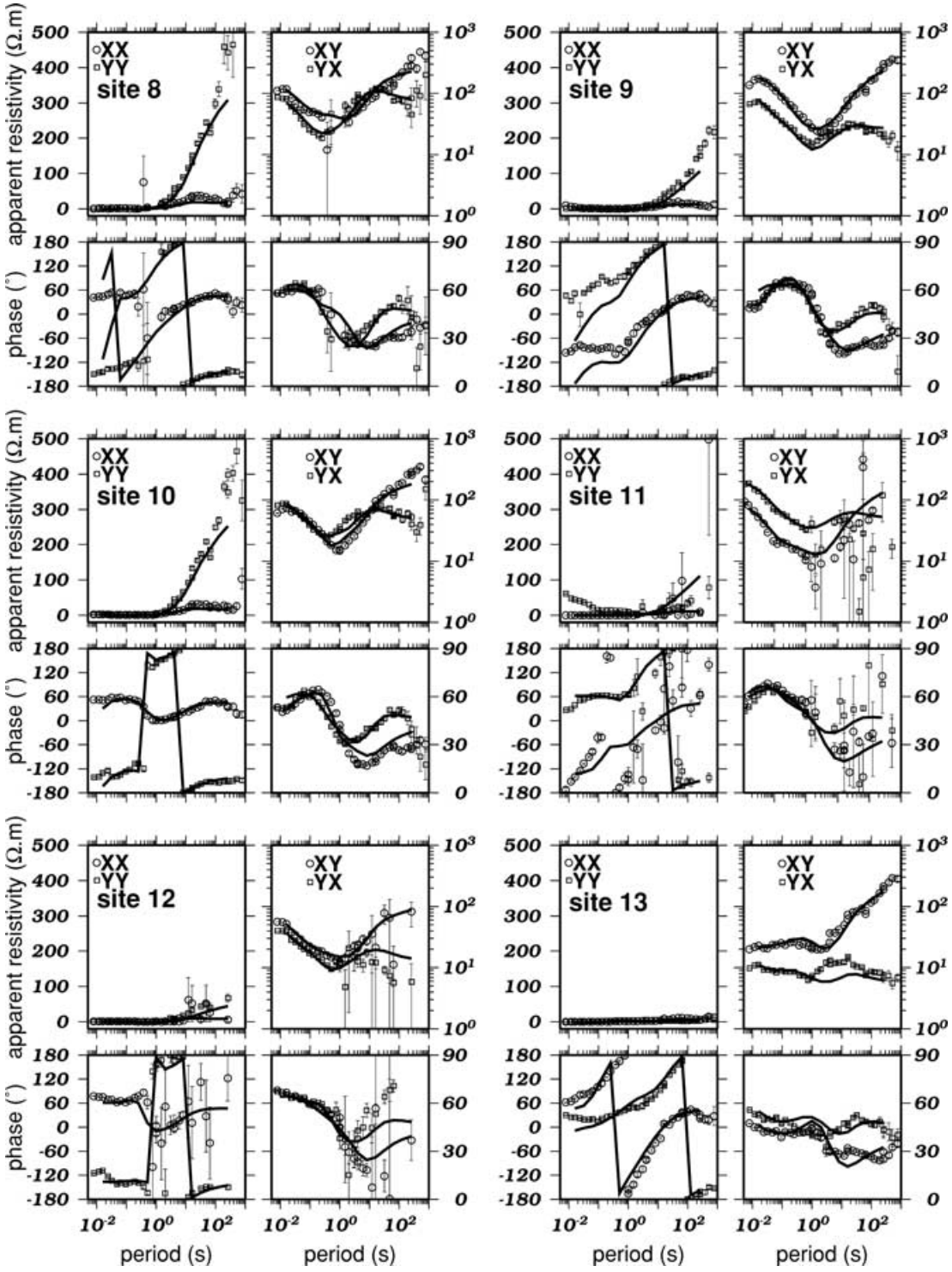

Figure 4. As for Fig. 3 for sites 8–13.

in the magnetic north, *x*, and east, *y*, directions. The station spacing varies between 1 and 3 km. It is a minimum along a roughly east–west gravity profile (Fig. 1) allowing an integrated geophysical interpretation. The other stations have a larger spacing and are distributed over the area for 3-D MT modelling. We deployed two stations simultaneously in order to allow cross remote-referencing for the computation of robust MT impedances.

The electric and magnetic field time-series were transformed into the frequency domain. The 2 × 2 MT impedance tensor **Z** relating the horizontal electric (Ex, Ey) to the horizontal magnetic (Bx, By) fields was determined using the robust remote reference method of Chave & Thompson (1989). The impedance tensors at the 20 sites are shown in Figs 3–6. Electric noise from power lines seriously affected the high frequency band MT impedance tensors (>128 Hz, not shown in Figs 3–6), and therefore they will not be considered further. However, the data in the longer period bands are of very good quality, leading to precise MT impedances with small error bars for periods up to 256 s. The data at the longest periods did

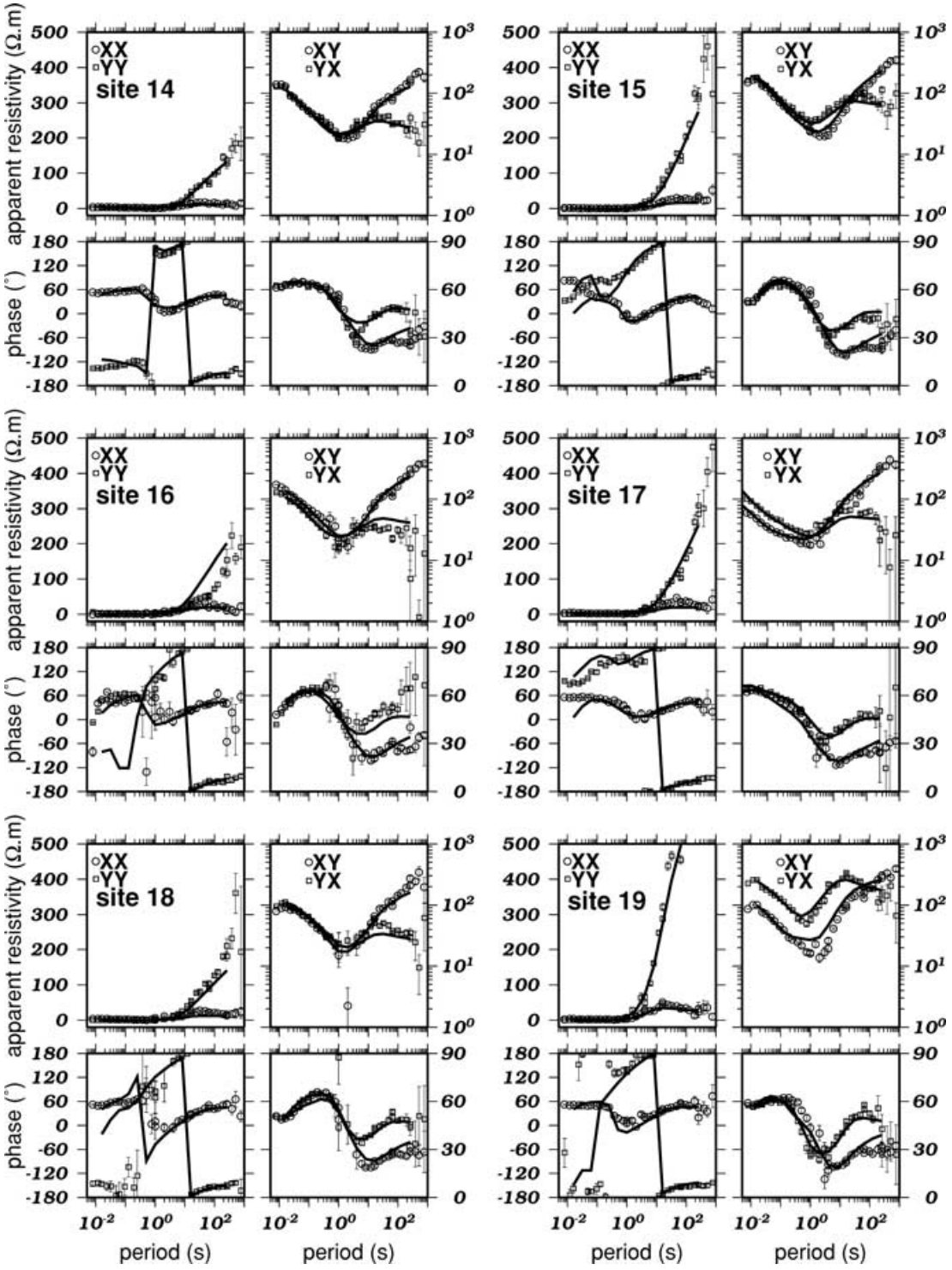

Figure 5. As for Fig. 3 for sites 14–19.

not always provide good transfer functions because of the limited recording time (20–24 hr).

3.2 Modelling

We calculated the maximum electrical direction (MED) at each site and each period. The MED is the rotation angle of the **E** field or **B** field axis that maximizes or minimizes the impedance tensor (Counil *et al.* 1986). In a 2-D geometry the MED corresponds to the strike of the structure or to the direction perpendicular to it, depending on the nature of the medium underneath. The MED for five sites, representative of the whole data set are shown as a function of period in Fig. 7(a). While a N30°–70° trend dominates at periods >2 s, there is no dominant trend at shorter periods indicating a full 3-D structure. Maps of the MED at periods of 0.125 s (Fig. 7b) and 12 s (Fig. 7c) show its spatial variation. The regional trend is visible at

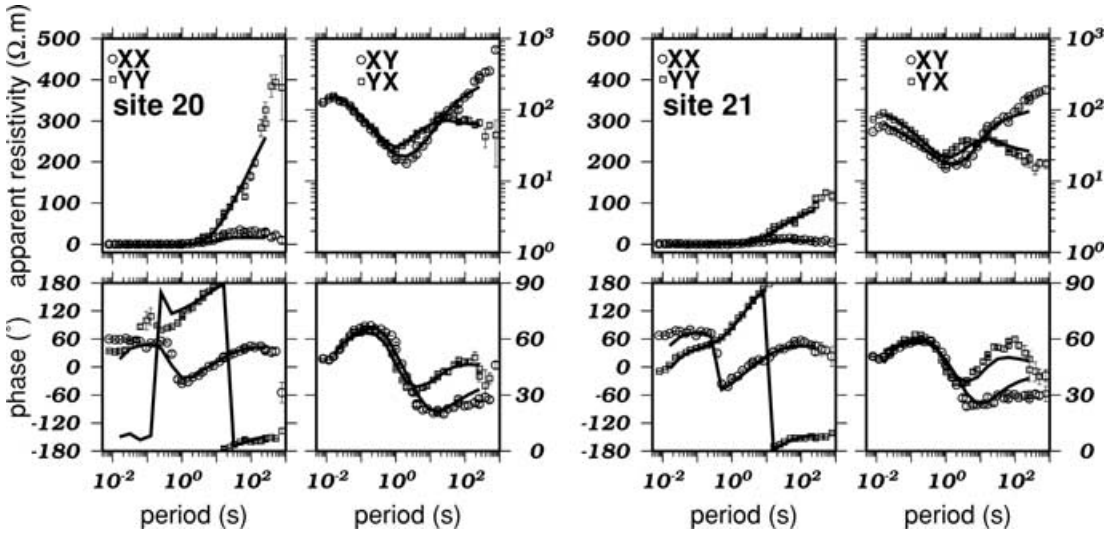

Figure 6. As for Fig. 3 for sites 20–21.

longer periods (Fig. 7c), but shallow structures locally change the MED at shorter periods (Fig. 7b), principally in the northern and southeastern areas.

We applied full tensor 3-D MT inversion using the approach of Hautot *et al.* (1999, 2000). The method is based on the minimization of the misfit between the data and the model response using a non-linear steepest gradient method. The forward problem is solved at each iteration with the 3-D finite difference algorithm proposed by Mackie *et al.* (1993). Here, we used a new version of their code (modified by Booker & Handong, private communication, 1999), that uses two polarized tangential fields on vertical edges tangential and normal to a source magnetic field, respectively. The boundary condition on the base of the model is the impedance of a homogeneous halfspace.

The 3-D model is parametrized by 11 blocks in the x direction, 9 blocks in the y direction (see horizontal grid in Fig. 8) and 12 layers in the vertical, z, direction. The starting model had an average horizontal layered earth over a half space (resistivities: 150, 10 and 150 ohm m; layer thicknesses: 600 and 1950 m) obtained from a 1-D analysis of the determinant average of the MT tensor (Ranganayaki 1984). After a number of iterations, the sizes of the blocks were adjusted by trial and error and the inversion was run again until a minimum misfit was reached. The final volume is 24.8 (x) × 19.3 (y) × 13.3 (z) km. For numerical reasons, we interpolated the data onto a set of 15 periods (256, 128, 64, 32, 16, 8, 4, 2, 1, 0.5, 0.25, 0.125, 0.0625, 0.03125 and 0.015625 s) for the inversion. The four complex elements of the impedance tensor at each site are inverted providing 2400 degrees of freedom. The model parameters are the resistivities of the blocks of the 3-D model. In areas of poor data coverage, some blocks have been amalgamated in order to reduce the number of parameters (Fig. 8). Layers 10 and 11 were found to have nearly identical resistivities and have also been combined. The final number of model parameters is 990.

The initial root-mean-square (rms) misfit of 55 was reduced to 3.9 for the best-fitting model. The rms misfit calculated for the off-diagonal terms only is close (3.2) to the total rms misfit (3.9), indicating that the four components of the MT tensor are approximately equally well modelled. The agreement between the data and the model responses for all sites is shown in Figs 3–6. The final 3-D resistivity distribution is shown in Fig. 8. Each panel shows the resistivity distribution in a layer of the model. In the top four layers (from the surface to 550 m), the resistivity distribution is quite heterogeneous, with large very resistive features separated by more conductive structures. Below, and down to 2.8 km depth, the layers are more conductive, containing small even more conductive bodies (resistivity <5 ohm m). Layers 10+11 (2.8–7.3 km depth) are substantially more resistive than those above. Below 7.3 km depth (layer 12), conductive features limit the eastern and western edges of the otherwise quite resistive medium.

Possible distortion of the electromagnetic field by the adjacent (electrically conductive) sea water (the coast effect) was *a posteriori* tested numerically following the approach of Menvielle *et al.* (1982). A digital 2 × 2 km topography and bathymetry map (ETOP 2001) was used to generate a heterogeneous thin sheet (HTS) of variable conductance (Fig. 9). The sea-side conductance was set to sea water conductivity (0.3 S m^{-1}) times the water depth. The land side conductance is small everywhere, so was assumed constant and equal to 1 s. The HTS topped a four layer 1-D model (from the surface, resistivities of 300, 50, 1000, 200 ohm m, thicknesses of 0.55, 2.25, 5.5m with the final layer a half-space) derived from the 3-D MT model. The electromagnetic field was computed at 1 Hz using the approach proposed by Vasseur & Weidelt (1977). At 1 Hz, the induction length Z/ω (where Z is the impedance tensor magnitude and ω is angular frequency) is 3-4 km. As expected (e.g. Menvielle *et al.* 1982), the inland horizontal magnetic field does not suffer from the coast effect. The horizontal electric field (Fig. 9) is marginally affected, particularly near the coastline. At frequencies higher than 1 Hz, the same calculation was carried out with a restricted water column height in order to satisfy the thin-sheet assumption. This is justified by a maximum water depth of 10–20 m at distances from the shore of up to 1 km, the induction length at 10 Hz. Again, the coast effect is found to be negligible. Thus, except for small (10–15 per cent) distortion at site 13, the nearest to the coast, all stations are unaffected at the frequencies of this survey.

3.3 Sensitivity analysis

As the result of the restricted number of periods used for the inversion and the choice of 3-D parametrization of the surveyed area,

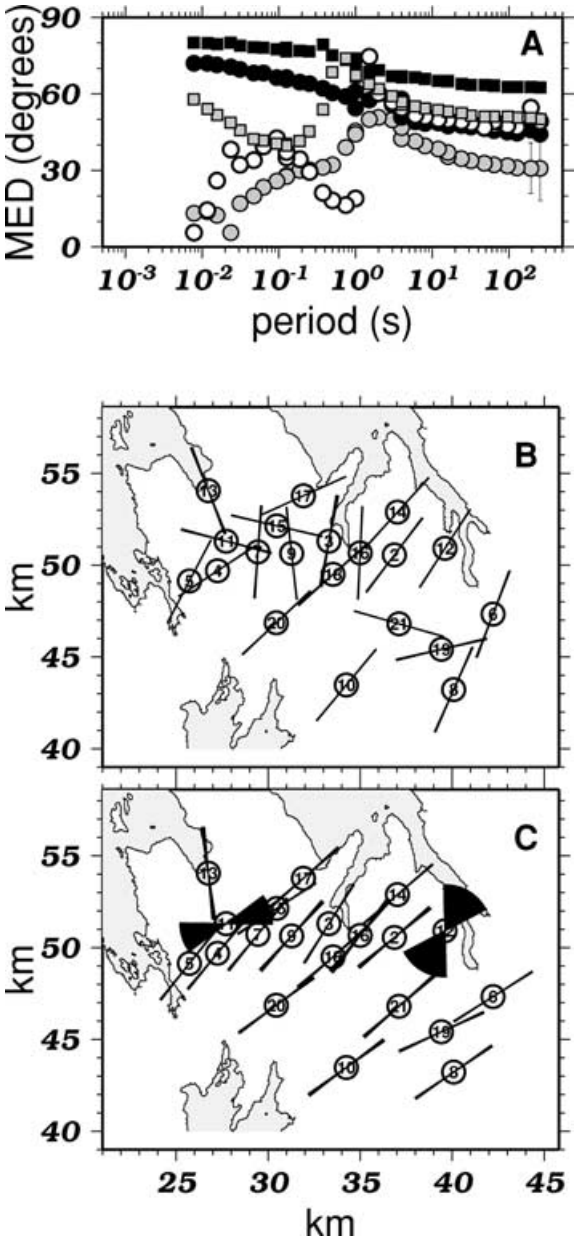

Figure 7. Maximum electrical direction (MED). (a) MED at five sites distributed over the surveyed area as a function of period. Sites 5 (grey circles), 17 (black circles), 2 (white circles), 19 (black squares), and 10 (grey squares). (b) MED at each site at period $T = 0.125$ s. The width of the pie wedge is one standard deviation. (c) Same as B at period $T = 12$ s.

the misfit obtained for the best-fitting model is not an absolute mimimum, but is some compromise between all sites, periods and data quality. Therefore, the parameters of the model may not be equally constrained by the data. The sensitivity of the data to the final model was tested with an analysis based on changing one parameter of the model while leaving the others constant and calculating the corresponding change in the misfit. Depending on its resolution, changing the resistivity in one block of the 3-D model may decrease or increase the misfit at all sites, but also may decrease the misfit at some sites and increase it at others. For every change in a model parameter, we used the following functions to decide whether that change is acceptable or not (Hautot *et al.* 2000):

$$(\Delta\mathrm{rms}^m)^2 = \frac{1}{N_s}\sum_{ls=1}^{N_s}\frac{\left[\chi^2_{ls}(m) - \chi^2_{ls}(0)\right]}{N_{95}}, \tag{1}$$

$$(\Delta\mathrm{rms}^+)^2 = \frac{1}{N_s}\sum_{ls=1}^{N_{sp}}\frac{\left\{\left[\chi^2_{ls}(m) - \chi^2_{ls}(0)\right] \geq 0\right\}}{N_{95}}, \tag{2}$$

$$(\Delta\mathrm{rms}^-)^2 = \frac{1}{N_s}\sum_{ls=1}^{N_{sm}}\frac{\left\{\left[\chi^2_{ls}(0) - \chi^2_{ls}(m)\right] > 0\right\}}{N_{95}}, \tag{3}$$

$$\varepsilon^+ = \Delta\mathrm{rms}^+/\mathrm{rms}^0,\ \varepsilon^- = \Delta\mathrm{rms}^-/\mathrm{rms}^0,$$
$$\varepsilon^m = \Delta\mathrm{rms}^m/\mathrm{rms}^0, \tag{4}$$

where χ^2 is the misfit estimator, N_s is the total number of sites and $N_{sp}(N_{sm})$ the number of sites where the misfit increases (decreases). (0) denotes the best-fitting model and (m) the modified model. N_{95} is the theoretical χ^2 misfit per site at the 95 per cent confidence level. Thus ε^- (ε^+) measures the fractional decrease (increase) in misfit per site, relative to the total number of sites. ε^m describes the total relative increase or decrease in misfit for all sites.

We used the average relative data amplitude error (3 per cent) as a threshold for ε^m and ε^+. Once this was exceeded, the parameter value was deemed unacceptable. The sensitivity to each block of the best-fitting model was tested in this way by increasing then decreasing its resistivity value until the threshold for ε^m and/or ε^+ was reached. The results are shown in Fig. 10 as the ratio between the initial resistivity value and the resistivity value corresponding to the threshold, which provides the acceptable resistivity range for each parameter. Thus, when the ratio is close to 1, the parameter is well constrained by the data while a large ratio indicates a poorly constrained parameter. It is necessary to refer to the resistivity model (Fig. 8) to better understand the sensitivity analysis results. Electromagnetic induction is more sensitive to conductive materials than to resistive materials. Thus, when the resistivity in a block is large, increasing its value might not affect the misfit (large ratio in Fig. 10, top) while decreasing it might significantly affect the misfit and thus might not be acceptable (small ratio in Fig. 10, bottom). The result in layer 10 + 11 ($z = 2.8$–7.3 km depth) provides an example. This layer is homogeneously resistive, and the absolute resistivity value is rather well constrained in the centre part of the layer. However, the upper limit of the resistivity value is poorly constrained in the northern and southern parts of the modelled area. This means that, there, the structure is resistive without a well defined upper value but cannot be conductive, as indicated by the small ratio values in Fig. 10, bottom.

A parameter is definitely not constrained when the ratio for both upper and lower limits is large. This is the case near the edges of the model in the uppermost layers (1–4) where the resistivity destribution is constrained by the electromagnetic field at (shorter) periods that attenuate rapidly both laterally and vertically. In contrast, long-period data integrate information over a large volume. The sensitivity analysis for layer 12 (7.3–13.3 km depth, Fig. 10) indicates poorly constrained resistivity values. However, this result was obtained by changing successively the resistivity value in each individual block, a change which represents a very local effect in this depth range. To test if the resistivity variation in layer 12 is reasonably constrained, the resistivity value in the whole layer was set to its average value (70 ohm m). The misfit at all sites increased dramatically ($\varepsilon^m = 66$ per cent). Similar results were obtained when the resistivity of each block was set to its value in the layer above

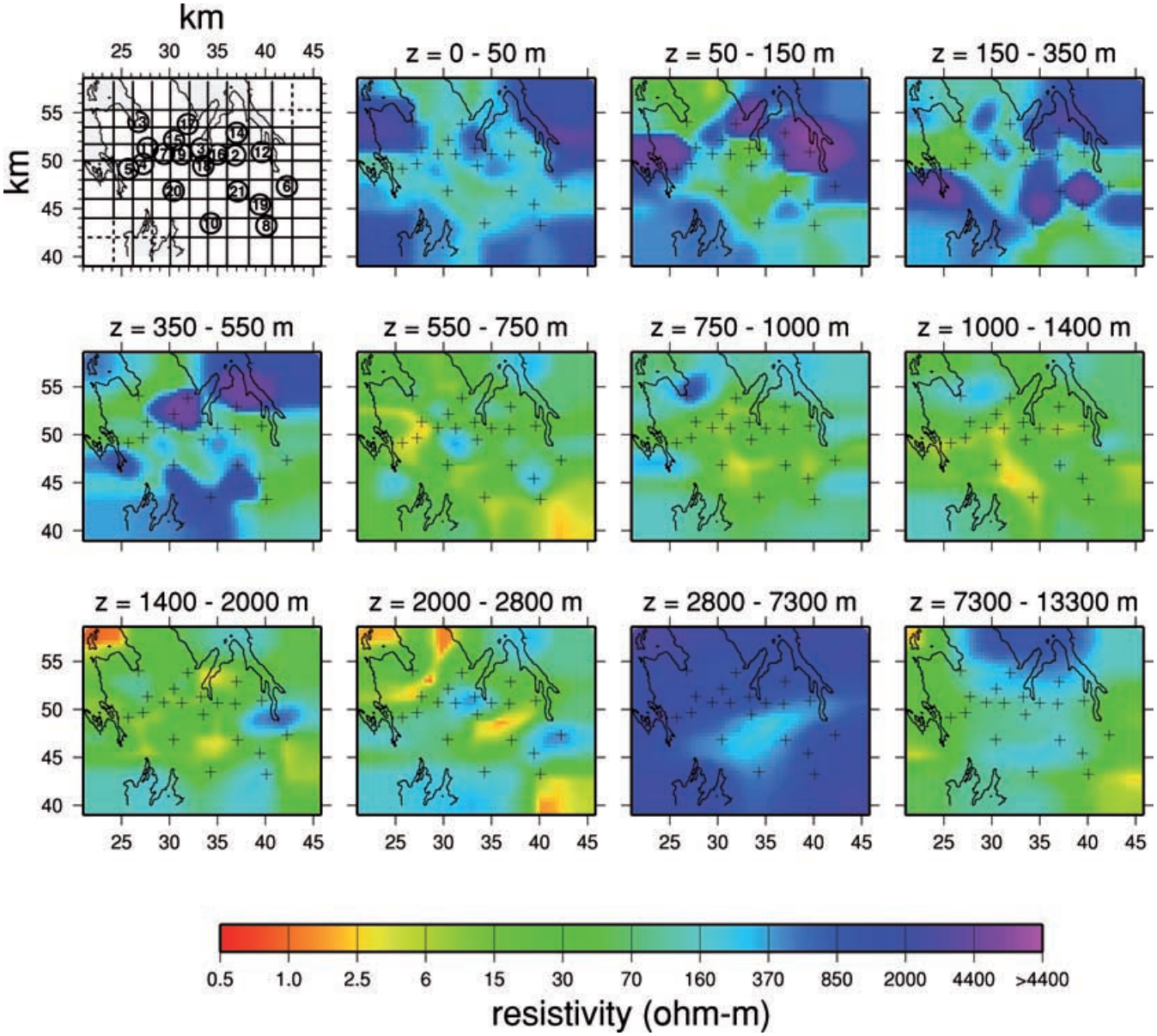

Figure 8. Resistivity maps for layers 1 to 12 of the best-fitting 3-D model (layers 10 and 11, 2800–7300 km depth, are combined; see text). The top left panel shows the site numbers and grid used. The dashed lines indicate the blocks that have been amalgamated during the inversion. Site locations are shown by crosses in subsequent panels.

(layer 10 + 11; $\varepsilon^m = 195$ per cent) or to a low value (10 ohm m; $\varepsilon^m = 62$ per cent). This means that the heterogeneity in layer 12 is required by the data.

Overall, it can be concluded from the sensitivity analysis that our best-fitting model is well constrained by the data, but must be interpreted carefully. It is reasonable to interpret local structures within the area covered by the sites down to 2.8 km depth (layer 9), but only the regional trend at the surface array scale below this.

4 INTERPRETATION OF THE 3-D RESISTIVITY MODEL

Seismic data and geological information from one borehole in the northern part of the resistivity model (Pentex Oil data, private communication) and information on the Skye lava field (Single & Jerram 2004) suggest that the resistivity decrease at ∼550 m corresponds to the contact between the volcanic series and the sedimentary formations, with the Mesozoic sedimentary structures below (depths 550–2800 m). Within the Mesozoic series, with an average resistivity of ∼30 ohm m, there are small-scale structures, both more resistive and more conductive, whose resistivity values are resolved (Fig. 10). The more resistive features (resistivity >100 ohm m) suggest either a thickening of the volcanic series or the presence of igneous sills intruded within the sediments. A similar resistivity contrast between intruded igneous material and sediments was observed in the Afar volcanic province (Hautot *et al.* 2006). Alternatively, in the deeper layers (depth >1400 m), the resistive features can reasonably be interpreted as lying below the Mesozoic series, giving an indication of the topography of its base. With the resistivity parameter only, it is difficult to put a structural interpretation on the conductive

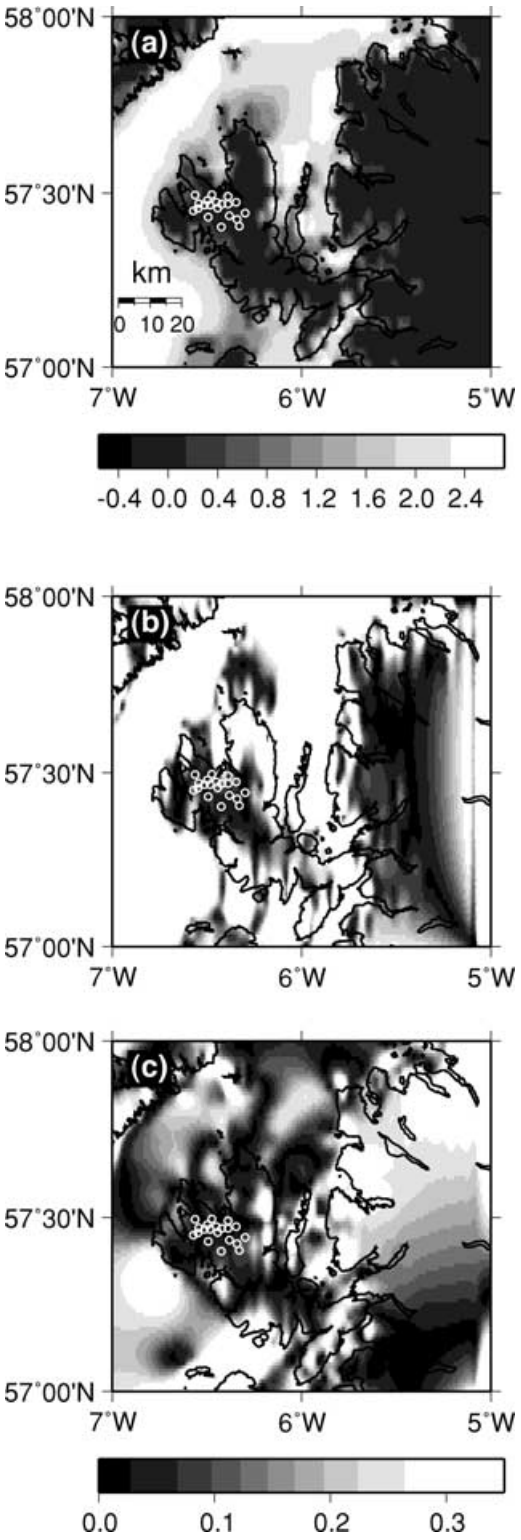

Figure 9. (a) The integrated conductivity model (in Siemens) for the coast effect calculation. The inducing magnetic source field is here in the E–W direction. (b) and (c): The difference between the electric field anywhere and the electric field in the centre of the site array (white circles) divided by the latter (so that the fraction is dimensionless). Hence, this factor represents the fractional coast effect anomalous electric field (AEF) in the N–S direction (b) and E–W direction (c) with respect to the centre of the site array. The AEF induced by a N–S magnetic source field (not presented here) showed a similar pattern.

features (resistivity <100 ohm m), so they will be discussed in the following section in conjunction with the gravity data. Nevertheless, the heterogeneous resistivity distribution agrees well with a fluviatile to lagoonal environment (Harris 1992). A massive marine series would result in a more homogeneous structure. No clear structural trend appears, except in layer 9, where the small-scale features, alternatively resistive and conductive, seem preferentially oriented along a NE–SW trend that agrees with the rifting extension direction (O'Neill & England 1994). The thickness of layer $10 + 11$ (2.8–7.3 km depth) is in agreement with the thick Precambrian Torridonian sandstones succession that deposited during an uplifting phase of the Lewisian basement (Stewart 1982; O'Neill & England 1994). Thus, the deeper layer could be associated with the Lewisian basement. If so, our model would provide the first image of the contact between the Torridanian succession and the Lewisian basement that cannot be observed anywhere on the island. The heterogeneous resistivity distribution observed below 7.3 km is compatible with the inhomogeneous structure of the sheared and folded Lewisian units (Mason & Brewer 2004), and the $\sim$NS trend of the resistivity contrast, between a resistive medium in the centre and conductive features on the western and eastern edges of the survey area, agrees with the NNE–SSW faults that controlled the formation of the Sea of Hebrides basin (Fig. 1).

5 INTEGRATED GEOPHYSICAL ANALYSIS

Between 2001 and 2003, 237 gravity stations were recorded within the survey area as part of the SIMBA project on integrated geoscience approaches to sub-basalt imaging (Williamson *et al.* 2002). The survey network spacing was designed in order to target the base of the basalt, and the average distance between stations was 250 m. The gravity values were earth-tide, latitude, free air, Bouguer and terrain corrected and each year's data set was tied to a common base station, giving Bouguer anomaly values with an accuracy of 0.2–0.25 mGal. They were then combined with British Geological Survey (BGS) gravity data, 14 stations with an approximate spacing of 2 km, to extend the gravity data set to an area matching that of the MT data and allow modelling of the regional gradient and deeper structure. BGS regional gravity stations in the Scottish highlands were established along roads and tracks, where available, and using helicopter transport in inaccessible areas. The BGS surveying of this region was mainly completed during the 1970s, and the corrections applied as above. The data processing is further described in the SIMBA project final report.

2-D gravity modelling was carried out along the approximately East-West profile shown in Fig. 1(b). A 2-D resistivity section along the profile was extracted from the resistivity volume (Fig. 11a) and used to generate the initial gravity model. The depths to the base of basalt, the sedimentary sequence and the Torridonian succession were inferred from the resistivity model (Fig. 11b). Density values were taken from results of previous work in the area and generally accepted values (e.g. O'Neill & England 1994). The resistivity section shows highly conductive bodies in the sedimentary sequence that may be indicative of zones of differing porosity and therefore density. Thus, the sedimentary layer in the gravity model was divided into zones of differing density. Overall, the gravity modelling was much improved by using the MT model as a guide to varying densities within the Mesozoic sediments and shallower structure. The improved gravity match shown in Fig. 11(c) was obtained with a high-density structure (density 2770 kg m^{-3}), possibly a sill complex, at the base of the basalt at a distance of 30 km along the profile

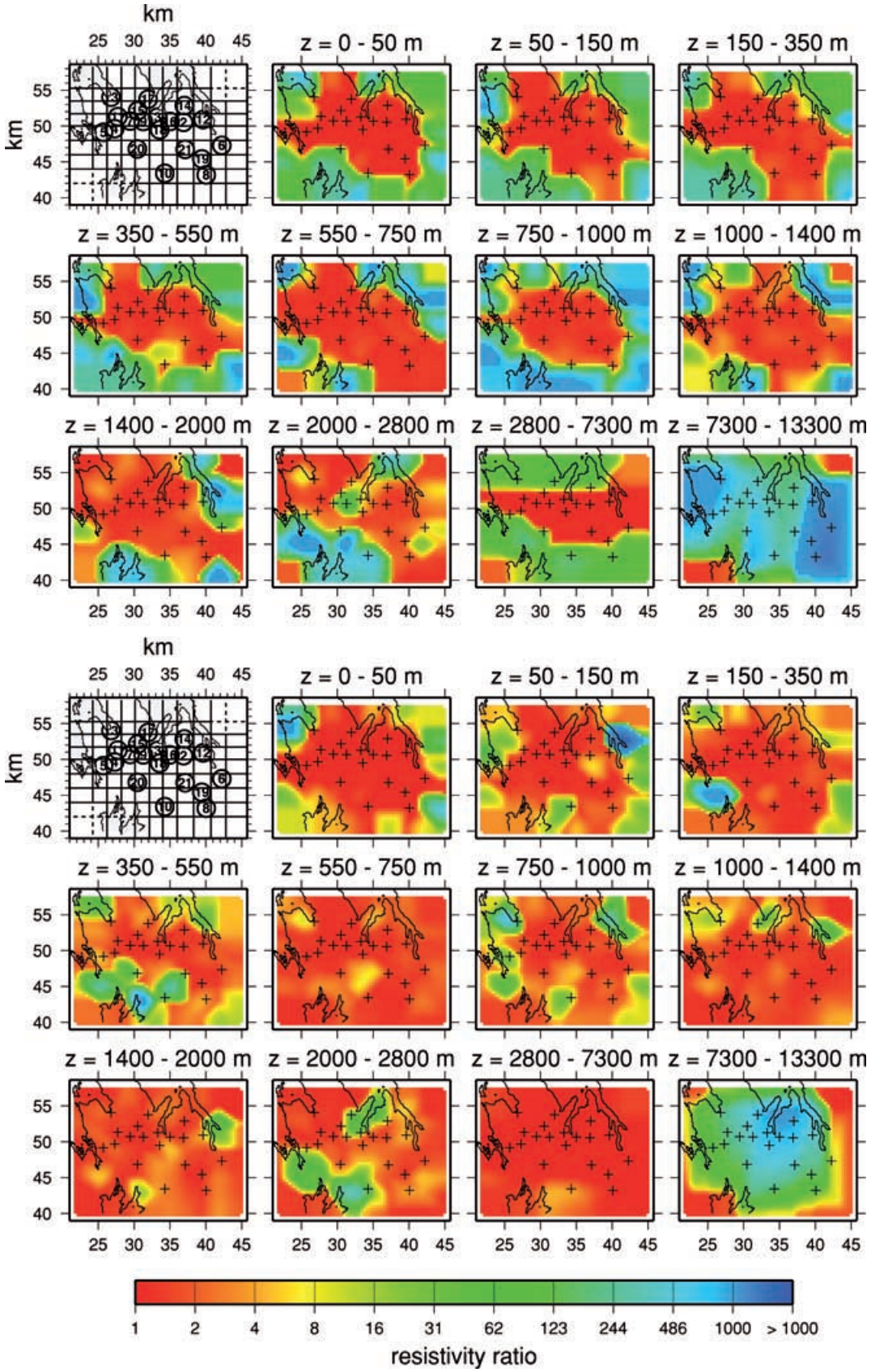

Figure 10. Results of the sensitivity analysis of the model shown in Fig. 8. The panels show the amount by which the resistivity of each block must be changed, relative to its value in the best-fitting model, for the parameters ε^{+} and/or ε^{m} to increase by 3 per cent. See text for further details. Top (bottom): results obtained when the resistivity is increased (decreased); the resistivity ratio is calculated with the best-fitting value in the denominator (numerator) so that the ratio always exceeds unity.

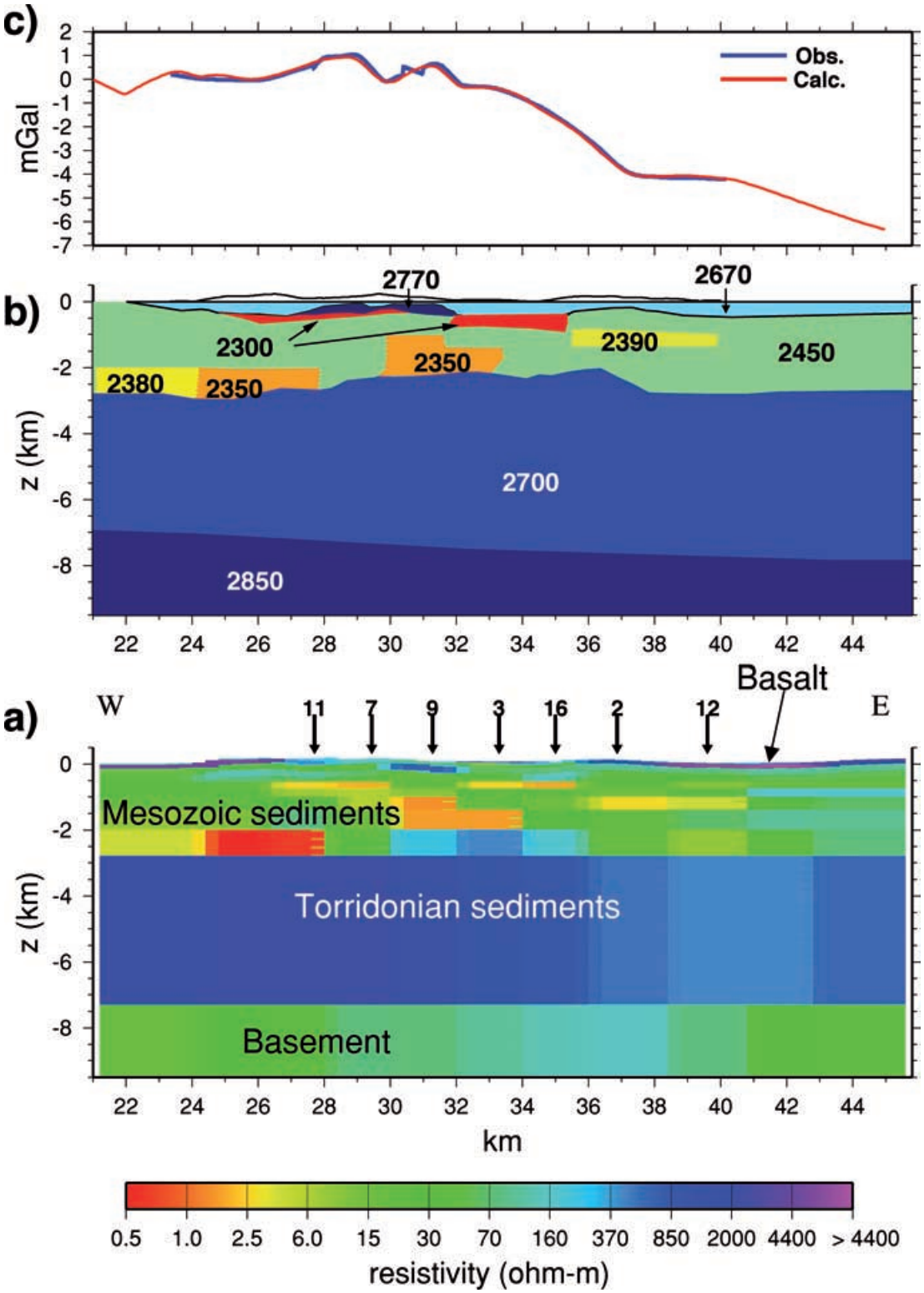

Figure 11. Results of the MT and gravity data integration. (a) Vertical resistivity cross-section extracted from the 3-D resistivity volume (Fig. 8) along the profile shown in Fig. 1(b). (b) 2-D gravity model derived from the resistivity model along the same profile. Density values are in kg.m^{-3}. (c) Observed (blue) and calculated (red) Bouguer gravity field values.

of Fig. 11(b), and a slightly modified depth to basalt and sediments. The flat top surface of the Torridonian sediments has been replaced by a ridge in the gravity model, inferred from the higher resistivities (similar to those of the Torridonian sediments) at depths 2–2.8 km beneath sites 9–16 in the resistivity model. The small-scale conductive features within the sedimentary sequence are modelled with low-density values which, combined with their low resistivity, suggest that the sediments have a locally enhanced porosity. In this

fluviatile and lagoonal environment, this could be interpreted as indicating sedimentary depocentres. On the other hand, the shallow resistive feature beneath site 9 is modelled with a high-density value, which can be interpreted as a sill intrusion within the sediments.

At increasing depths, the gravity data resolution deteriorates and the more regionally spaced BGS values are the main gravity control on the model. The deepening of the top Lewisian basement from west to east can be justified by a long-wavelength trend in the gravity profile. However, this gravity trend could be the result of a number of scenarios: a deepening basement, lateral density variations within the Torridonian and/or Lewisian basement or even deeper variations in density or structure. In this case, we have tentatively placed the Torridanian/Lewisan interface at a depth of approximately 7 km based on the resistivity boundary, and introduced a slight west to east slope to account for the regional gravity trend. The MT data do not have the sensitivity to distinguish between this and the horizontal basement surface of Fig. 11(a). The deeper structure requires further constraints for accurate gravity modelling; however, in this case, where the focus is on the shallower basalts and sediments, our model offers an explanation of the longer wavelength anomalies within the gravity profile.

6 CONCLUSION

The results of this case study show that 3-D MT inversion is an appropriate tool for the characterization of flood basalt provinces, here applied in a volcanic margin context on the Isle of Skye. Our resistivity model provides an image of the sedimentary sequence down to the basement, 13 km deep. The sediments are covered by Tertiary lava flows, a few hundred metres thick that prevent seismic data interpretation for deep structures in this type of environment (O'Neill & England 1994). An integrated MT and gravity study is used to infer the structures respresented by small-scale features in the sedimentary sequence of the 3-D resistivity model. Resistivity variation can be interpreted in terms of porosity variation as demonstrated by gravity modelling and geological mapping of facies variations within the lava sequence (Single & Jerram 2004). This suggests that the resolution of 3-D MT imaging is sufficiently accurate to interpret sedimentary bodies in terms of depositional environment which provides additional benefit in terms of locating higher porosity bodies in the exploration context. Implications are important for geological and geodynamical studies, but also for resource potential assessment.

ACKNOWLEDGMENTS

This work was supported by funding provided by the EU 5th Framework Project SIMBA (contract no. ENK6-CT-2000-00075). S.H. was supported by the European Community through a Marie Curie Fellowship (contract #2001-1669). The BGS is thanked for allowing use of their gravity data. SPAM equipment was loaned by NERC Geophysical Equipment Facility (loan #708). The assistance of G. Cairns, E. Legge Smith, M. Quemeneur, W. Vetel, and W. Wilson is acknowledged during the fieldwork. We thank the two anonymous reviewers for their useful comments and suggestions, contributor no. 1031 of the IVEM, European Institute for Marine. Studies, (Brest, France).

REFERENCES

Chave, A.D. & Thompson, D.J., 1989. Some comments on magnetotelluric response function estimation, *J. Geophys. Res.,* **94,** 14 202–14 215.

Counil, J.L., Le Mouël, J.L. & Menvielle, M., 1986. Associate and conjugate direction concepts in magnetotellurics, *Ann. Geophys.,* **4,** 115–130.

Durham, M.J. (Ed.), 2003. Structural framework of the North Sea and Atlantic Margin, *2003 edition map, Petroleum Exploration Society of Great Britain*.

England, R.W., Butler, R.W.H. & Hutton, D.H., 1993. The role of Palaeocene magmatism in the Tertiary evolution of basins on the NW seaboard, in *Petroleum Geology of Northwest Europe: Proceedings of the 4th Conference*, pp. 97–105, ed. Parker, J.R., The Geological Society, London.

ETOPO2, U.S. Department of Commerce, National Oceanic and Atmospheric Administration, National Geophysical Data Center, 2001. 2-minute Gridded Global Relief Data.

Fliedner, M.M. & White, R.S., 2001. Seismic structure of basalt flows from surface seismic data, borehole measurements and synthetic seismogram modelling, *Geophysics,* **66,** 6, 1925–1936.

Hamilton, M.A., Pearson, D.G., Thompson, R.N., Kelley, S.P. & Emeleus, C.H., 1998. Rapid eruption of Skye lavas inferred from precise U-Pb and Ar-Ar dating of the Rum and Cuillin plutonic complexes, *Nature,* **394,** 260–263.

Harris, J.P., 1992. Mid-Jurassic lagoonal delta systems in the Hebridean basins: thickness and facies distribution patterns of potential reservoir bodies, in *Basins on the Atlantic seaboard: Petroleum geology, sedimentology and basin evolution*, pp. 111–144, ed. Parnell, J., Geological Society special publication No 62.

Hautot, S., Tarits, P. & Tarits, C., 1999. Electromagnetic imaging of fissured crystalline bedrock in hydrogeology, in *Three-Dimensional Electromagnetics, Geophysi. Dev. Ser.,* Vol. 7, pp. 525–541, eds Oristaglio M. & Spies, B., Society of Exploration Geophysicists, Tulsa, Okla.

Hautot, S., Tarits, P., Whaler, K.A., Le Gall, B., Tiercelin, J.J. & Le Turdu, C., 2000. The deep structure of the Baringo Rift basin (central Kenya) from 3-D magneto-telluric imaging: Implications for rift evolution, *J. geophys. Res.,* **105,** 23 493–23 518.

Hautot, S., Whaler, K.A., Gebru, W. & Dessissa M., 2006. The structure of a Mesozoic basin beneath the Lake Tana area, Ethiopia, revealed by magnetotelluric imaging, *J. Afr. Earth Sci.,* **44**(3), 331–338, 10.1016/j.jafrearsci.2005.11.027.

Hinz, K., Eldholm, O., Block, M. & Skogseid, J., 1993. Evolution of North Atlantic volcanic continental margins, in *Petroleum Geology of Northwest Europe: Proceedings of the 4th Conference*, pp. 901–913, ed. Parker, J.R., The Geological Society, London.

Jerram, D.A., 2002. Volcanology and facies architecture of flood basalts, in *Volcanic Rifted Margins: Geological Society of America Special Paper 362*, pp. 119–132, eds Menzies, M.A., Klemperer, S.L., Ebinger, C.J. & Baker, J.

Jerram, D.A. & Widdowson, M., 2005. The anatomy of Continental Flood Basalt Provinces: Geological constraints on the processes and products of flood volcanism, *Lithos,* **79,** 385–405.

Kumar, D., Ravi Bastia, R. & Debajyoti Guha, D., 2004. Prospect hunting below Deccan basalt: imaging challenges and solutions, *First Break,* **22,** 35–39.

Mackie, R.L., Madden, T.R. & Wannamaker, P.E., 1993. Three-dimensional magnetotelluric modelling using difference equations—Theory and comparisons to integral equation solutions, *Geophysics,* **58,** 215–226.

Martini, F., Hobbs, R.W., Bean, C.J. & Single, R., 2005. A complex 3-D volume for subbasalt imaging, *First Break,* **23,** 41–51.

Mason, A.J. & Brewer, T.S., 2004. Mafic dyke remnants in the Lewisian Complex of the Outer Hebrides, NW scotland: a geochemical record of continental break-up and re-assembly, *Precambrian Research,* **133,** 121–141.

Menvielle, M., Rossignol, J.C. & Tarits, P., 1982. The coast-effect in terms of deviated electric currents: a numerical study, *Phys. Earth planet. Inter.,* **28,** 118–128.

Menzies, M.A., Klemperer, S.L., Ebinger, C.J. & Baker, J., 2002. eds Menzies, M.A., Klemperer, S.L., Ebinger, C.J. & Baker, J., *Volcanic Rifted Margins. Geol. Soc. Amer. Spec. Pap.,* **362,** 230 pp.

O'Neill, P.S. & England, R.W., 1994. The structure of the Sea of Hebrides Basin: an integrated gravity and seismic model, *Scottish J. Geol.,* **30,** 1–9.

Pearson, D.G., Emeleus, C.H. & Kelley, S.P., 1996. Precise 40Ar/39Ar age for the initiation of Palaeogene volcanism in the Inner Hebrides and its regional significance, *J. geol. Soc. Lond.,* **153,** 815–818.

Ranganayaki, R.P., 1984. An interpretive analysis of magnetotelluric data, *Geophysics,* **49,** 1730–1748.

Ritter, O., Junge, A. & Dawes, G.J.K., 1998. New equipment and processing for magnetotelluric remote reference observations, *Geophys. J. Int.,* **132,** 535–548.

Single, R.T. & Jerram, D.A., 2004. The 3-D facies architecture of flood basalt provinces and their internal heterogeneity: examples from the Palaeogene Skye Lava Field, *J. geol. Soc. Lond,,* **161,** 911–926.

Stein, A.M. & Blundell, D.J., 1990. Geological inheritance and crustal dynamics of the northwest Scottish Continental Shelf, *Tectonophysics,* **173,** 455–467.

Stewart, A.D., 1982. Late Proterozoic rifting in NW Scotland: the genesis of the 'Torridonian', *J. geol. Soc. Lond.,* **139,** 413–420.

Vasseur, G. & Weidelt, P., 1977. Bimodal electromagnetic induction in non-uniform thin sheets with an application to northern Pyrenean induction anomaly, *Geophys. J. R. astr. Soc.,* **51,** 669–690.

Williamson, I.T. & Bell, B.R., 1994. The Palaeocene lava field of west-central Skye, Scotland: Stratigraphy, palaeogeography and structure, *Trans. Royal Soc. of Edinburgh: Earth Sciences,* **85,** 39–75.

Williamson, P. & the SIMBA Project Personnel, 2002. SIMBA: integrated geoscience approaches to subbasalt imaging, *Subbasalt imaging, J. of Conf. Abst.,* **7,** 201, Cambridge Publications.

Ziegler, P.A. & Cloetingh, S., 2004. Dynamic processes controlling evolution of rifted basins *Earth-Science Rev.,* **64,** 1–50.